

Impedance Matching in Photovoltaic Systems Using Cascaded Boost Converters and Sliding-Mode Control

Reham Haroun, *Student Member, IEEE*, Abdelali El Aroudi, *Member, IEEE*, Angel Cid-Pastor, *Member, IEEE*, Germain Garica, *Member, IEEE*, Carlos Olalla, *Member, IEEE*, and Luis Martínez-Salamero, *Senior Member, IEEE*

Abstract—Switching dc–dc converters are widely used to interface the dc output of renewable energy resources with power distribution systems in order to facilitate the use of energy at the customer side. In the case of residential photovoltaic (PV) applications, high conversion ratio is usually required, in order to adapt the low output voltages of PV modules to a dc bus voltage, while dealing with the appropriate impedance matching. In this paper, a system connected to a PV panel consisting of two cascaded dc–dc boost converters under sliding-mode control and working as loss-free resistors is studied. The modeling, simulation, and design of the system are addressed. First, an ideal reduced-order sliding-mode dynamics model is derived from the full-order switched model taking into account the sliding constraints, the nonlinear characteristic of the PV module, and the dynamics of the MPPT controller. For this model, a design-oriented averaged model is obtained and its dynamic behavior is analyzed showing that the system is asymptotically globally stable. Moreover, the proposed system can achieve a high conversion ratio with an efficiency close to 95% for a wide range of working power. Numerical simulations and experimental results corroborate the theoretical analysis and illustrate the advantages of this architecture in PV systems.

Index Terms—Cascaded boost converters, impedance matching, loss-free resistor (LFR), MPPT, photovoltaic (PV) systems, sliding-mode control (SMC).

I. INTRODUCTION

CLEAN renewable energy resources have been given increasing interest in recent years, due to concerns about global warming and its related harmful greenhouse effect, air quality, and sustainable development [1]. In the future power grid, not only the utilities, but also the users can produce electric energy by aggregating distributed generation sources [2]. In

Manuscript received January 20, 2014; revised April 30, 2014; accepted July 7, 2014. Date of publication July 14, 2014; date of current version January 16, 2015. This work was supported in part by the Spanish *Ministerio de Educación e Innovación* under Grants DPI2010-16481, DPI2010-16084, CSD2009-00046, and DPI2013-47293-R, under Grant FI/DGR2011 FI/B 00990 by the Commissioner for Universities and Research of the Government of Catalonia and by the European Social Fund, and by the Generalitat de Catalunya, Beatriu de Pinós programme under Award BP-B00047. Recommended for publication by Associate Editor C. Fernandez.

R. Haroun, A. El Aroudi, A. Cid-Pastor, C. Olalla, and L. Martínez-Salamero are with the Departament d'Enginyeria Electrònica, Elèctrica i Automàtica, Escola Tècnica Superior d'Enginyeria, Universitat Rovira i Virgili 43007, Tarragona Spain (e-mail: reham.haroun@urv.cat; abdelali.elaroudi@urv.cat; angel.cid@urv.cat; carlos.olalla@urv.cat; luis.martinez@urv.cat).

G. García is with the LAAS-CNRS, University of Toulouse, Toulouse 31062, France (e-mail: garcia@laas.fr).

Color versions of one or more of the figures in this paper are available online at <http://ieeexplore.ieee.org>.

Digital Object Identifier 10.1109/TPEL.2014.2339134

that context, photovoltaic (PV) arrays, wind turbines, and batteries are used to feed a main (dc or ac) bus connected to its loads, as well as the utility grid, forming the so-called nanogrid system [3]. Nanogrids can then work in the stand-alone mode or they can be connected to the utility grid performing peak shaving and smooth transitions between the different modes of operation.

While the realization of the nanogrids of the future remains an open question, it seems that dc distribution systems will present several advantages with respect to ac systems, despite the cheaper protection circuit breakers and lower maintenance costs of the latter. First, dc systems are more efficient and can provide higher power quality with lower harmonics [4], [5]. Second, a significant advantage of the dc-based approach is the fact that power handling can be completely uninterrupted by having switched-mode power converters featuring the current limit [6], allowing the eventual aggregation of distributed generation sources to the main dc grid [3], [7]. In such a context, the future home electric system is foreseen to have two dc voltage levels: a main dc bus of high voltage (380 V) powering major home appliances and electric vehicle charging, and a low dc voltage bus (48 V) for supplying computer loads, low power consumer electronics or lighting [8]–[11].

The interconnection of residential scale PV systems to such a main dc bus can typically be carried out by two approaches. The first one consists of connecting the series string(s) of PV modules to a central power converter, which allows us to avoid high-step up conversion ratios, with the disadvantages of high sensitivity to mismatch induced loss and losses due to a centralized MPPT. The second one employs a power converter for each module, in order to perform high granularity maximum power point tracking (MPPT), which provides higher flexibility in system layout, lower sensitivity to shading, better protection of PV sources, redundancy in case of failures, and easier and safer installation and maintenance, besides of data gathering [12]. However, the converter per module approach can present difficulties for achieving the desired output voltage under mismatched conditions of some PV modules, when converters are connected in series at the output [13]. As an alternative, PV modules can be connected in parallel to the dc bus. In such a case, one of the key technology issues is the implementation of a power converter that interfaces the possibly low voltage and power of the PV module to the main voltage dc distribution bus of 380 V. For this reason, it is necessary to have an adaptation stage with a high-voltage conversion ratio (above 10) in addition

to good static and dynamic performances, which should guarantee a good impedance matching of the PV generator regardless of the load variations and/or the weather conditions like fast moving clouds, temperature changes or even shadowing effects.

The design of such a high-gain converter is not a simple task. Challenges include high conversion efficiency, small number of components, reliability, and high dynamic performance, resulting in appropriate MPPT accuracy and tracking speed [14]–[17]. Single-stage solutions can provide high efficiency. However, they present limitations in the conversion ratio due to the finite commutation times of the power devices and the size of the passive elements. A possible method to deal with these problems is the inclusion of a step-up transformer. This is the usual approach in dc–ac applications where the step-up converter supplies an inverter [18]. However, the inclusion of a transformer limits the frequency of operation and introduces switching surges in the circuit. A recently explored single-stage alternative is the use of coupled inductors as proposed in [19]–[22]. This method was shown to be able to adapt a low voltage from a PV generator to a dc voltage of 200 V with conversion efficiencies exceeding 95%. Nevertheless, its large input current ripple imposes the use of an electrolytic capacitor with a high capacitance value in parallel with the PV generator, so that the voltage ripple does not affect the MPPT accuracy [14], [15], which in turn can compromise reliability [16]. Finally, Z-source converter has been proposed as an alternative for high-gain conversion [23], but this topology has a limited conversion efficiency as reported in [24].

In this paper, we propose the use of a two-stage approach based on a cascade connection of two boost converters. While this provides large conversion ratios and continuous input current, the expected efficiency is low. In addition, the cascaded connection of power converters has some inherent drawbacks regarding controller design and dynamic stability of the system, which can be tackled with well-known *impedance ratio* criteria by Middlebrook [25]. We overcome these two problems as follows. First, we will show that, although, conversion efficiencies are lower than those presented in [20], [21], this structure can provide efficiencies well above 90% for an output voltage of 380 V. Note that this structure can take advantage of novel silicon carbide (SiC) diodes with breakdown voltages above 400 V, effectively reducing the reverse recovery losses of the second stage. Second, the dynamic stability is ensured with the use of a sliding-mode control approach [26], [27] based on the loss-free resistor (LFR) concept [28], which was proven to be particularly advantageous in terms of robustness and performance in [29]. This method allows us to avoid the classical frequency response approach shown in [25], which is only valid around the operating point of the analysis. The sliding-mode approach provides a stable regulation regardless of uncertainty and the inherent nonlinearities of the dynamics of switching dc–dc converters.

Previous literature dealing with two cascaded boost converters for PVs can be found in [30] and [31]. While [30] analyzed its efficiency, [31] demonstrated the global stability of the two cascaded boost converters using different canonical elements with a certain choice of MPPT controller output. This paper extends the results of this last paper [31], including the nonlinear voltage–current characteristic of the PV module, the dynamics

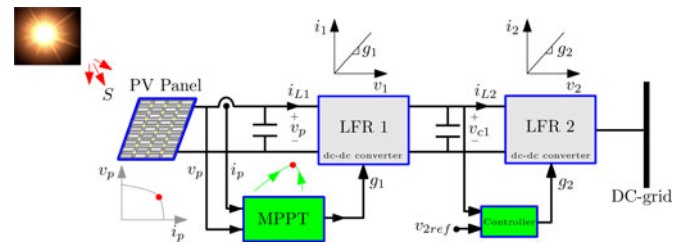


Fig. 1. Dc grid connected to a PV module through cascaded dc–dc converters.

of the MPPT algorithm, and the nonlinear dynamics of the cascaded system with the proposed sliding-mode controller (SMC). Besides, experimental results showing efficiency measurements and demonstrating the advantages of the dynamic performance of this approach are provided.

The rest of this paper is organized as follows. Section I presents the problem of the impedance matching and proposes a possible solution through a cascade connection of two boost converters behaving as LFRs. The extremum seeking control (ESC) MPPT is briefly reviewed in the same section. Section II describes the system under study and the mathematical modeling of the system is addressed. In addition, its stability analysis is carried out in the same section. In order to evaluate the reported system, a comparison will be carried out between the proposed system and a high step-up converter using coupled inductors in Section V. Moreover, the theoretical predictions and associated numerical simulations of the proposed system are presented in the same section. Experimental validation is provided in Section V. Finally, the conclusions of this study are summarized in Section VI.

II. SYSTEM OVERVIEW

The proposed conversion system is based on two cascaded boost converters behaving as LFRs as shown in Fig. 1. This section describes briefly the different parts of the system, the impedance matching of the PV characteristic, the realization of an SMC to obtain the LFR characteristic, and the MPPT circuit.

A. Impedance Matching in PV Systems

The switching converters can be used as an interface element to connect a PV generator to a load. Fig. 3 illustrates the problem of matching a PV generator to a dc load using two cascaded boost converters working as LFRs. An LFR is a two-port element which is characterized by its input current being proportional to the input voltage. The power absorbed by this input port is virtually transferred to the output without losses, i.e., the output port has an inherent power source characteristic [32], [33]. The output power can be expressed as a function of the LFR conductance $g_1 = 1/r_1$

$$P_o = P_i = g_1 v_p^2. \quad (1)$$

As a consequence, due to the feedback loop in the input side, the output power is not influenced by the output port variables as it can be shown in Fig. 2(b) [34]. This inherent characteristic

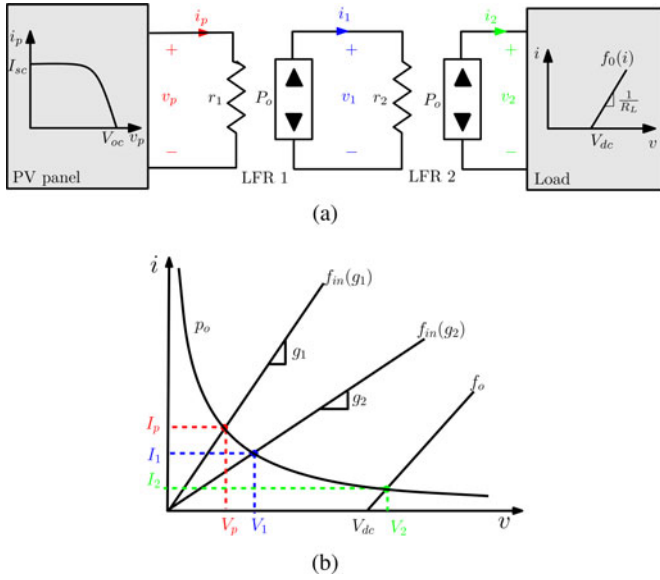


Fig. 2. Impedance matching of a PV module generator to a dc load using two cascaded boost-based LFRs. (a) Block diagram. (b) Power source characteristics of the LFR output port.

of LFRs is of high importance to avoid the influence of the load variations in the impedance matching of PV systems. The LFR element does not exist naturally but its synthesis can be carried out by using a switched mode converter [35]. Under specific conditions regarding sliding-mode operation and stability, the proportionality between the voltage and the current at the input port can be guaranteed in steady-state.

Both PV generator and load have been modeled in the first quadrant i - v characteristic. The dc load can be modeled by means of a function $i_2 = f_o(v_2)$, which corresponds to the one-port description of the usual dc loads such as batteries, LED lamps, electrolytic cells, etc., and can be expressed generally by

$$v_2 = f_o(i_2) = V_{dc} + i_2 R_L \quad (2)$$

where $V_{dc} > 0$ and $R_L > 0$. The analysis of the impedance matching will be carried out by considering a very small equivalent series resistance ($R_L \simeq 0$) and with a nominal dc voltage V_{dc} much greater than the open-circuit voltage V_{oc} of the PV module.

The PV module current-voltage characteristic and the LFR steady-state input impedance are depicted in Fig. 3. Note that there is no operating point that would result from the direct connection of the PV generator and the dc bus since there is no intersection between their respective characteristics ($V_{dc} \gg V_{oc}$). It can be observed that conductance g can naturally be used to set up the operating point of the PV module as illustrated in Fig. 3. Operating points A and B correspond, respectively, to conductances g_a and g_b with $g_a > g_b$. The LFR converters can operate at the optimal value of the conductance that leads to an intersection of the PV i - v characteristic curve and the LFR load line ($i = gv$) described by $f_{in}(g_{opt})$ at the MPP.

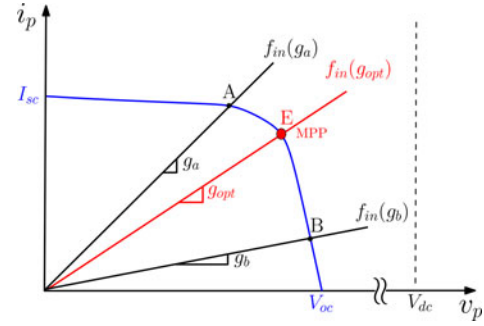


Fig. 3. PV module operating points for an impedance matching between the PV generator and the LFR.

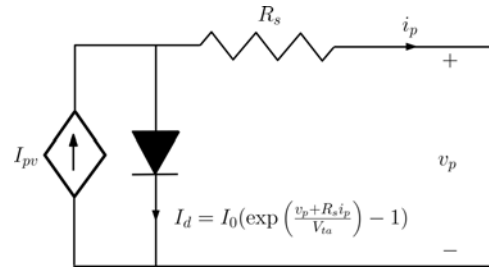


Fig. 4. Equivalent circuit diagram of the PV module model.

According to the current-voltage characteristic of the PV module, Fig. 4 shows an equivalent circuit whose output current can be expressed as follows [36], [37]:

$$i_p = I_{pv} - I_0 \left(\exp \left(\frac{v_p + R_s i_p}{V_{ta}} \right) - 1 \right) \quad (3)$$

where v_p is the voltage of the module, I_{pv} and I_0 are the photo-generated and saturation currents, respectively, V_{ta} is the thermal voltage which is given by $V_{ta} = N_s A K T / q$ where A is the diode quality factor, K is the Boltzmann constant, q is the charge of the electron, T is the PV module temperature, and N_s is the number of the cells connected in series.

In addition, the photogenerated current I_{pv} depends on the irradiance and temperature as follows:

$$I_{pv} = I_{sc} \frac{S}{S_n} + C_t (T - T_n) \quad (4)$$

where I_{sc} is the short-circuit current, T_n and S_n are the nominal temperature and irradiance, S is the ambient irradiance, and C_t is the temperature coefficient.

The implicit equation (3) can be transformed to an explicit relation using the Lambert-W function, as in [38]. In this way, a nonlinear relationship between the current i_p and the voltage v_p at the basic PV unit terminals can be obtained and expressed as follows:

$$i_p = I_{pv} + I_0 - \frac{V_{ta}}{R_s} \mathcal{W} \left(\frac{R_s I_0}{V_{ta}} \exp \left(\frac{v_p + R_s (I_{pv} + I_0)}{V_{ta}} \right) \right) \quad (5)$$

where \mathcal{W} stands for the Lambert-W function. This equation is used in the analysis of the system that follows.

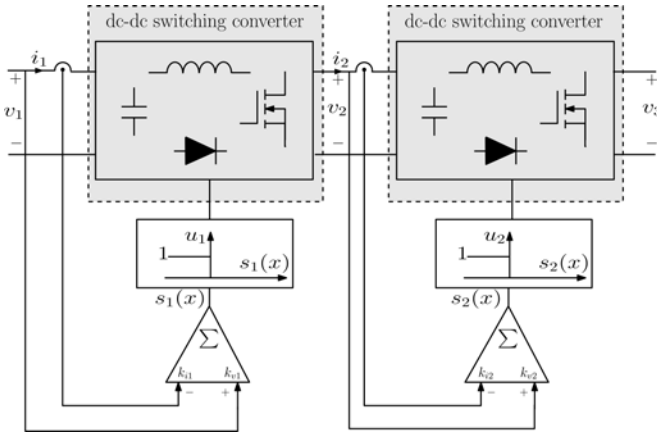


Fig. 5. Block diagram of two cascaded switching converters to synthesize a LFR at the input of each converter.

B. Synthesis of LFR in Sliding-Mode Regime

Fig. 5 shows the block diagram of two cascaded switching converters, which under an appropriate SMC behave as LFRs. In this figure, the switching functions for the two converters are given by

$$s_1(\mathbf{x}) = k_{v1}v_1 - k_{i1}i_1 \quad (6)$$

$$s_2(\mathbf{x}) = k_{v2}v_2 - k_{i2}i_2 \quad (7)$$

where i_1 , v_1 , i_2 , and v_2 are the instantaneous input and intermediate currents and voltages, respectively. In the steady-state operation, the switching functions become zero. Therefore, the following relations between the steady-state variables are obtained:

$$s_1(\mathbf{x}) = 0 \Rightarrow I_1 = g_1 V_1, g_1 = \frac{k_{v1}}{k_{i1}} \quad (8)$$

$$s_2(\mathbf{x}) = 0 \Rightarrow I_2 = g_2 V_2, g_2 = \frac{k_{v2}}{k_{i2}} \quad (9)$$

where I_1 , V_1 , I_2 , and V_2 are the steady-state-averaged values of the input and intermediate currents and voltages, respectively. In practice, the control strategy is given by a hysteresis control law with the following output values:

$$u_i(t) = \begin{cases} 0, & \text{if } s_i(t) > +h \text{ or } |s_i(t)| < h \text{ and } s_i(t^-) = +h \\ 1, & \text{if } s_i(t) < -h \text{ or } |s_i(t)| < h \text{ and } s_i(t^-) = -h \end{cases} \quad (10)$$

where s_i is the switching function which is also the input to the hysteresis controller of the stage i and t^- is the last instant when the control signal hit the switching boundaries defined by $\pm h$. It has to be pointed out that the presence of a hysteresis comparator (HC) in the feedback loop of each stage of Fig. 5 results in a variable switching frequency which depends mainly on the hysteresis width h and the operating point [39].

A possible circuit configuration of this system with the cascaded boost converters and the PV module is depicted in Fig. 6. The circuit consists of two cascaded boost converters with their corresponding SMC. The first sliding surface is described by the switching function $s_1(\mathbf{x}) = g_1 v_p - i_p$ for the first stage,

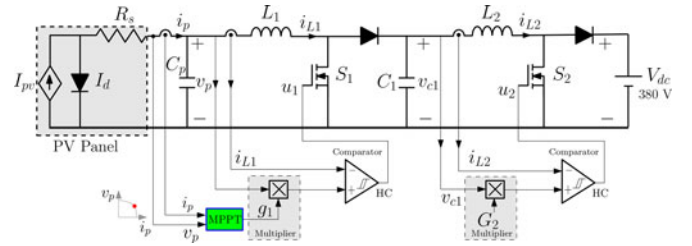


Fig. 6. Schematic diagram of two cascaded boost-based LFRs under SMC.

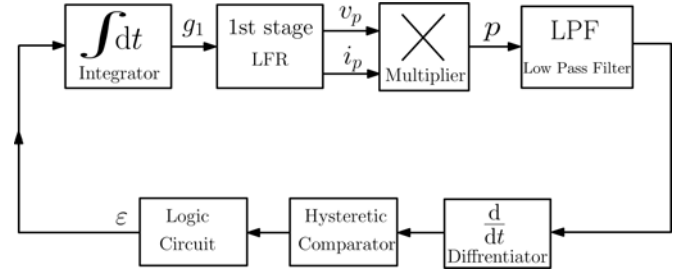


Fig. 7. Generation of the conductance g_1 by means of an MPPT scheme based on ESC.

which establishes the steady-state relationship between the voltage of the module v_p and the input current i_p , where g_1 is the output of the MPPT controller. The second sliding surface for the second stage is described by the switching function $s_2(\mathbf{x}) = g_2 v_{c1} - i_{L2}$ which establishes the relationship between the intermediate voltage v_{c1} and the intermediate current i_{L2} where $g_2 = G_2$ is a constant coefficient.

C. Maximum Power Point Tracking

The goal of the MPPT circuit is to ensure that the PV module always operates at its MPP regardless of the temperature, insolation, and load variation. A number of tracking algorithms have been applied for different types of dc-dc converter topologies [40]–[43]. ESC, whose block diagram is shown in Fig. 7, is one of the commonly used types of MPPT algorithms which can force the PV system to approach the MPP by increasing or decreasing a suitable control variable. While the figure shows a well-known architecture [43], it is worth to point out a few aspects which are relevant to the stability analysis. The HC provides a binary signal that indicates whether the power-time derivative is positive or negative. This signal is introduced into a logic circuit with an inhibition delay τ_d which establishes, after a fixed time interval, if the direction of maximum searching ϵ has to be maintained or should be changed. The waiting interval ensures that the converter is operating in steady-state when the decision on the change or maintenance of the control law sign is made. Thus, in the proposed scheme, the settling time of the PV voltage and current are directly related to the capacitor C_p and the loss-free resistance r_1 as it can be easily deduced from Fig. 6. The minimum time delay τ_d can then be defined as

$$\tau_d \geq 5r_{1,\max}C_p \quad (11)$$

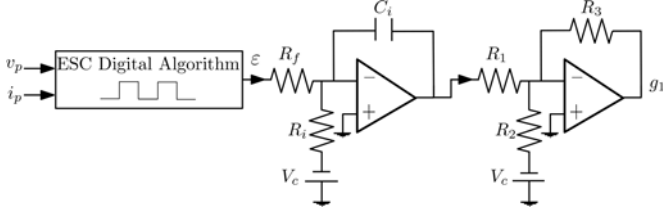


Fig. 8. Simplified description of an ESC MPPT: a digital algorithm, an integrator, and a gain.

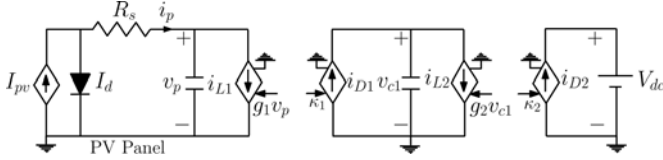


Fig. 9. Large-signal circuit corresponding to the ideal sliding dynamics where $\kappa_1 = g_1 v_p^2 / \beta_2 / v_{c1}$, $\kappa_2 = G_2 v_{c1}^2 / V_{dc}$.

where $r_{1,\max}$ is the maximum value that should be achieved by the MPPT algorithm. Note that this maximum value can be found by considering the point where the PV characteristic presents the MPP at the highest current and the lowest voltage, which corresponds to the highest irradiation level and temperature.

In the proposed model, the MPPT algorithm is described by a square wave generator that can be implemented by a microcontroller and an integrator as shown in Fig. 8. From this figure, the output g_1 of the ESC MPPT controller can be described as

$$g_1 = k_1 V_c - \frac{k_2}{\tau_1} \int_0^t v_s(\zeta) d\zeta \quad (12)$$

where $v_s = k_3 V_c - \varepsilon$, $\tau_1 = R_f C_i$, $k_1 = R_3 / R_2$, $k_2 = R_3 / R_1$, $k_3 = R_f / R_i$, and V_c is a constant voltage source.

III. MATHEMATICAL MODELING AND STABILITY ANALYSIS

A. Switched Model

By applying Kirchhoff's voltage and current laws to the circuit depicted in Fig. 6, the following set of differential equations describing the system dynamical behavior are obtained:

$$\frac{di_{L1}}{dt} = \frac{v_p}{L_1} - \frac{v_{c1}}{L_1}(1 - u_1) \quad (13)$$

$$\frac{di_{L2}}{dt} = \frac{v_{c1}}{L_2} - \frac{V_{dc}}{L_2}(1 - u_2) \quad (14)$$

$$\frac{dv_p}{dt} = \frac{i_p}{C_p} - \frac{i_{L1}}{C_p} \quad (15)$$

$$\frac{dv_{c1}}{dt} = \frac{i_{L1}}{C_1}(1 - u_1) - \frac{i_{L2}}{C_1} \quad (16)$$

where for the first stage (respectively, second stage) $u_1 = 1$ when the switch S_1 (respectively, S_2) is closed and $u_1 = 0$ when the switch S_1 (respectively, S_2) is open. All the parameters that appear in (13)–(16) are shown in Fig. 6.

B. Equivalent Control

A reduced-order dynamical model can be obtained from the full-order switched model by substituting the discontinuous binary signals u_1 and u_2 by their equivalent continuous variables $u_{eq1}(\mathbf{x})$ and $u_{eq2}(\mathbf{x})$ and taking into account the order reduction imposed by the sliding manifolds. These equivalent control variables are obtained by imposing that the trajectories are evolving on the switching manifolds and therefore one has $s_1(\mathbf{x}) = \dot{s}_1(\mathbf{x}) = \mathbf{0}$ and $s_2(\mathbf{x}) = \dot{s}_2(\mathbf{x}) = \mathbf{0}$. Therefore, the following set of equations defining the sliding-mode dynamics are obtained:

$$s_1(\mathbf{x}) = g_1 v_p - i_{L1} = 0 \quad (17)$$

$$s_2(\mathbf{x}) = G_2 v_{c1} - i_{L2} = 0 \quad (18)$$

$$\dot{s}_1(\mathbf{x}) = g_1 \frac{dv_p}{dt} + v_p \frac{dg_1}{dt} - \frac{di_{L1}}{dt} = 0 \quad (19)$$

$$\dot{s}_2(\mathbf{x}) = G_2 \frac{dv_{c1}}{dt} - \frac{di_{L2}}{dt} = 0. \quad (20)$$

Under sliding-mode conditions, the equivalent control variables $u_{eq1}(\mathbf{x})$ and $u_{eq2}(\mathbf{x})$ represent the control laws that describe the behavior of the system restricted to the switching surfaces where the system motion takes place on an average. Hence, from (13)–(16) and (19)–(20), $u_{eq1}(\mathbf{x})$ and $u_{eq2}(\mathbf{x})$ can be expressed as follows:

$$u_{eq1} = 1 - \frac{v_d}{v_{c1}} - \frac{v_m}{v_{c1}} \quad (21)$$

$$u_{eq2} = 1 - \frac{1}{V_{dc}} \left(v_{c1} + \alpha_2 \left(G_2 v_{c1} + \frac{g_1 v_p v_d}{v_{c1}} \right) \right) \quad (22)$$

where $\alpha_1 = g_1 L_1 / C_p$, $\alpha_2 = G_2 L_2 / C_1$, $v_d = v_p - \alpha_1 (i_p - g_1 v_p)$, and $v_m = v_p L_1 (k_2 (k_3 V_c - \varepsilon) / \tau_1)$. Note that the equivalent control variables u_{eq1} and u_{eq2} must be bounded between the minimum and the maximum values of u_1 and u_2 , respectively, i.e.

$$0 \leq u_{eq1} \leq 1 \text{ and } 0 \leq u_{eq2} \leq 1. \quad (23)$$

C. Sliding-Mode Conditions and Ideal Dynamics

By imposing the existence conditions given by (23), the sliding-mode domain can be obtained. For instance, in the plane (v_p, v_{c1}) and based on (21)–(23), the sliding-mode regime exists provided that $v_{c1L} < v_{c1} < v_{c2L}$, where the critical values v_{c1L} and v_{c2L} are given by

$$v_{c1L} = v_d + v_m \quad (24)$$

$$v_{c2L} = \frac{V_{dc} + \sqrt{V_{dc}^2 + 4\alpha_2 g_1 v_p (1 - \alpha_2 G_2)(v_d + v_m)}}{2(1 - \alpha_2 G_2)}. \quad (25)$$

Other boundaries also exist but the ones expressed by (24) and (25) are the most restrictive. The equivalent control variables $u_{eq1}(\mathbf{x})$ and $u_{eq2}(\mathbf{x})$ depend on g_1 , which is the output of the MPPT algorithm. Introducing (21) and (22) into (13)–(16) and considering (17)–(20) result in the following reduced-order model for the ideal sliding-mode dynamics:

$$\frac{dv_p}{dt} = \frac{i_p}{C_p} - \frac{g_1 v_p}{C_p} \quad (26)$$

$$\frac{dv_{c1}}{dt} = \frac{g_1 v_p^2}{C_1 v_{c1}} \beta_2 + \frac{\alpha_1 g_1 v_p}{C_1 v_{c1}} (g_1 v_p - i_p) - \frac{G_2 v_{c1}}{C_1} \quad (27)$$

$$\frac{dg_1}{dt} = -k_2 \frac{k_3 V_c - \varepsilon}{\tau_1} \quad (28)$$

where $\beta_2 = 1 + k_2 v_s L_1 / \tau_1$. The large-signal ideal sliding-mode dynamics given in (26)–(28) can be represented by the circuit depicted in Fig. 9. This model will be used for numerical simulations after its validation by the full-order switched model given in (13)–(16). The advantage of using this large-signal reduced-order model is the significant consumption time reduction if compared to the switched model. The inductor currents can be modeled by voltage controlled current sources which are governed by $g_1 v_p$ and $G_2 v_{c1}$ as mentioned in the switching surface equations. It is worth showing that the second term in (27) is very small. Therefore, to simplify the large-signal model block diagram, this term has been neglected.

D. Design-Oriented Averaged Model

The previous model (26)–(28) is a switched model whose dynamical behavior characterization is challenging due to the presence of the MPPT dynamics which introduce a switching variable ε and also due to nonlinearities. As a first step for stability analysis, averaging of the previous equations (26)–(28) over one period $2\tau_d$ is carried out, where τ_d is the delay period used in the MPPT controller. Let \bar{v}_p , \bar{i}_p , \bar{v}_{c1} , \bar{v}_s , \bar{g}_1 , and $\bar{\varepsilon}$ stand for averaged quantities, i.e.

$$\bar{\varepsilon} = \frac{1}{2\tau_d} \int_t^{t+2\tau_d} \varepsilon(\zeta) d\zeta \quad (29)$$

with similar expressions for the rest of averaged variables. Therefore, we obtain the following $2\tau_d$ -averaged equations:

$$\frac{d\bar{v}_p}{dt} = \frac{\bar{i}_p}{C_p} - \frac{\bar{g}_1 \bar{v}_p}{C_p} \quad (30)$$

$$\begin{aligned} \frac{d\bar{v}_{c1}}{dt} &= \frac{\bar{g}_1 \bar{v}_p^2}{C_1 \bar{v}_{c1}} \beta_2 + \frac{\alpha_1 \bar{g}_1 \bar{v}_p}{C_1 \bar{v}_{c1}} (\bar{g}_1 \bar{v}_p - \bar{i}_p) - \frac{G_2 \bar{v}_{c1}}{C_1} \\ \frac{d\bar{g}_1}{dt} &= -k_2 \frac{k_3 V_c - \bar{\varepsilon}}{\tau_1}. \end{aligned} \quad (31)$$

The next step in our study will be the determination of the equilibrium point of the averaged model defined in (30)–(31).

1) *Equilibrium Point*: The equilibrium point can be obtained by forcing the time derivative of the state variables of the averaged model to be null. In order to get an explicit expression of the equilibrium point, let us suppose that $R_s = 0$ in (3) which becomes

$$i_p = I_{pv} - I_0 \left(\exp\left(\frac{v_p}{V_{ta}}\right) - 1 \right). \quad (32)$$

From (30)–(31) and taking into account (17) and (18), the equilibrium point of the averaged-model is given by

$$x^* = [\bar{V}_p, \bar{V}_{c1}, \bar{G}_1]^\top = \left[\frac{\bar{I}_e}{\bar{G}_1}, \frac{\bar{I}_e}{\sqrt{\bar{G}_1 G_2}}, k_1 V_c \right]^\top \quad (33)$$

where $^\top$ stands for the transpose of a vector and \bar{I}_e can be expressed as follows:

$$\bar{I}_e = I_{pv} + I_0 - \bar{G}_1 V_t \mathcal{W} \left(\frac{I_0}{\bar{G}_1 V_{ta}} \exp\left(\frac{I_{pv} + I_0}{\bar{G}_1 V_t}\right) \right). \quad (34)$$

In order to validate the previous analytical expression for the equilibrium point, it has been calculated numerically by an iterating procedure with the exact expression (5) and using the analytical approximated expression given in (33) and a good agreement has been obtained for a wide range of practical parameter values.

The averaged values of the control variables at the equilibrium point can be obtained by substituting (33) in (21) and (22) and leads to the following expressions:

$$\bar{u}_{eq1}(x^*) = 1 - \sqrt{\frac{G_2}{\bar{G}_1}} \quad (35)$$

$$\bar{u}_{eq2}(x^*) = 1 - \frac{\bar{I}_p}{V_{dc}} \left(\frac{1}{\sqrt{\bar{G}_1 G_2}} - 2\alpha_2 \sqrt{\frac{G_2}{\bar{G}_1}} \right). \quad (36)$$

As mentioned previously in (23), $\bar{u}_{eq1}(x^*)$ and $\bar{u}_{eq2}(x^*)$ must be bounded between 0 and 1. Moreover, in steady-state, $\bar{I}_p = \bar{I}_{L1}$. Therefore, from (23), the following condition must be satisfied:

$$\bar{G}_1 > \max \left(G_2, \frac{(1 - 2\alpha_2 G_2)^2 I_p^2}{G_2 V_{dc}^2} \right). \quad (37)$$

It is worth to note that the previous condition (37) has been derived considering that $\bar{I}_p - \bar{G}_1 \bar{V}_p = 0$ at the equilibrium point.

2) *Small-Signal Stability Analysis*: In order to study the stability of the system, the nonlinear equations (30)–(31) are first linearized around the equilibrium point x^* given by (33), obtaining the following expression of the Jacobian matrix \mathbf{J} :

$$\mathbf{J} = \begin{pmatrix} -\delta & 0 & -\frac{\bar{V}_p}{C_p} \\ \beta_3 + \beta_1 (2\bar{v}_s + \frac{\partial \bar{\varepsilon}}{\partial \bar{v}_p}) - \beta_4 \frac{\bar{V}_p^2}{C_1 \bar{V}_{c1}} (\beta_2 + \alpha_1 \bar{G}_1) & & \\ -\frac{k_2}{\tau_1} \frac{\partial \bar{\varepsilon}}{\partial \bar{v}_p} & 0 & 0 \end{pmatrix} \quad (38)$$

where the parameters δ , \mathcal{L} , β_1 , β_2 , β_3 , and β_4 are given by

$$\delta = \frac{R_s \bar{G}_1 (1 + \mathcal{L}) + \mathcal{L}}{R_s C_p (1 + \mathcal{L})} \quad (39)$$

$$\mathcal{L} = \mathcal{W} \left(\frac{R_s I_0}{V_{ta}} \exp\left(\frac{\bar{V}_p + R_s (I_{pv} + I_0)}{V_{ta}}\right) \right) \quad (40)$$

$$\beta_1 = \frac{\sqrt{\bar{G}_1 G_2} L_1 k_2}{C_1 \tau_1}, \quad \beta_2 = \left(1 + k_2 \bar{V}_s \frac{L_1}{\tau_1} \right) \quad (41)$$

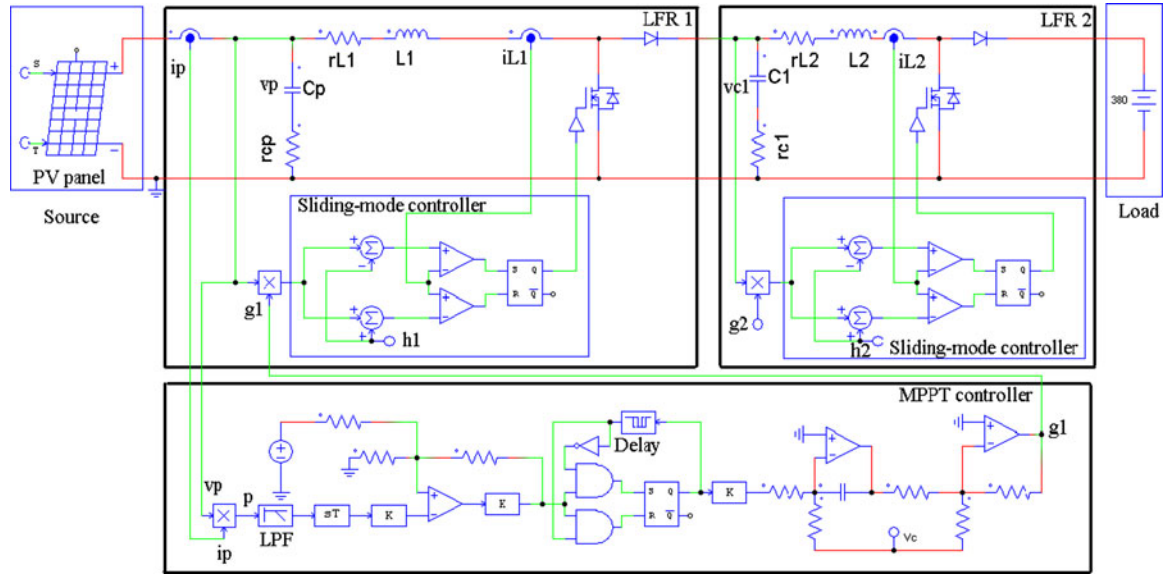


Fig. 10. PSIM schematic diagram of the two cascaded boost-based LFRs connected to a PV module operating with an ESC MPPT controller.

$$\beta_3 = \frac{1}{C_1} \left(2\bar{G}_1 - \sqrt{\bar{G}_1 \bar{G}_2 \delta} \right), \beta_4 = \frac{2G_2}{C_1} + \sqrt{\frac{G_2}{G_1}} \beta_1. \quad (42)$$

The characteristic polynomial equation of the linearized system is given by $\det(\mathbf{J} - s\mathbf{I}) = 0$, where \mathbf{I} is the unitary matrix. Developing this equation, the characteristic polynomial can be written in the following form:

$$s^3 + (\delta + \beta_4)s^2 + \delta\beta_4s - \frac{\bar{v}_p}{C_p} \frac{k_2}{\tau_1} \frac{\partial \bar{\varepsilon}}{\partial \bar{v}_p} s - \frac{\bar{v}_p}{C_p} \frac{k_2}{\tau_1} \frac{\partial \bar{\varepsilon}}{\partial \bar{v}_p} \beta_4 = 0. \quad (43)$$

Observe that we cannot study the stability of the system using the previous characteristic polynomial due to the nonavailability of an explicit mathematical expression of $\bar{\varepsilon}$ in terms of \bar{v}_p allowing a general result. It might be possible, however, to treat the system using numerical simulations. This has the advantage of not requiring such a mathematical expression as in the case of an analytical stability analysis. Fortunately, in our system, the averaged variable $\bar{\varepsilon}$ changes very slowly with respect to \bar{v}_p . Therefore, it can be considered that $\partial \bar{\varepsilon} / \partial \bar{v}_p \approx 0$ which implies that the characteristic polynomial can be simplified as follows:

$$s^2 + (\delta + \beta_4)s + \delta\beta_4. \quad (44)$$

This new simplified expression of the characteristic polynomial has two roots δ and β_4 located both in the left half plane, and hence, the equilibrium point of the averaged system is asymptotically stable. Note, however, that the previous stability analysis is only valid locally near enough to the equilibrium point. However, as the MPPT controller is included in the dynamical model, the equilibrium point corresponds to the MPP. This is because at the MPP one has $d\bar{p}/d\bar{v}_p \approx 0$, which implies that $d\bar{p}/dt \approx 0$, i.e., $d\bar{v}_p/dt \approx 0$ and $d\bar{i}_p/dt \approx 0$. If the stability is guaranteed for this point, it becomes inherently an attractor of the system. As the equilibrium point is unique, this ensures that it is a global attractor for the system. The following section pro-

 TABLE I
 PARAMETERS OF THE PV MODULE

Parameter	Value
Number of cells N_s	36 cell
Standard light intensity S_0	1000 W/m ²
Ref temperature T_{ref}	25 °C
Series resistance R_s	0.008 Ω
Short-circuit current I_{sc0}	5 A
Saturation current I_{s0}	3.8074·10 ⁻⁸ A
Band energy E_g	1.12
Ideality factor A	1.2
Temperature coefficient C_t	0.00065 A/C
Open-circuit voltage v_{oc}	22 V

vides numerical simulations showing that the basin of attraction of this equilibrium point is indeed very large.

IV. NUMERICAL SIMULATIONS

In order to verify the previous theoretical results, the original switched-mode system is simulated in PSIM using the schematic shown in Fig. 10. The PSIM solar module has an open-circuit voltage around 22 V based on the data of BP585, its internal parameters being shown in Table I. Note that the input voltage depends on the weather conditions and varies between 0 V and open-circuit voltage with a nominal MPP value of 18 V. Table II shows the rest of the system parameters. It has to be mentioned that the conductance G_2 has been selected in such a way that both stages work with approximately the same duty cycle, which in this case corresponds to a conversion ratio of 5 for each stage, or equivalently an intermediate voltage v_{c1} around 80 V. It is worth mentioning also that the parasitic elements have been included in the PSIM simulation shown in Fig. 10. They are the internal resistance of the inductors ($r_{L1} = 60$ mΩ and $r_{L2} = 130$ mΩ), the ON resistance of the MOSFETs ($r_{on1} = 60$ mΩ and

TABLE II
USED PARAMETER VALUES FOR THIS STUDY

L_1	L_2	C_p	C_1	G_2	h_1	h_2	k_1	k_2	k_3	τ_1	τ_d	V_c	f_s
200 μ H	2 mH	100 μ F	10 μ F	0.008 S	0.4 A	0.2 A	0.05	0.167	0.5	0.1 s	5 ms	5 V	50 kHz

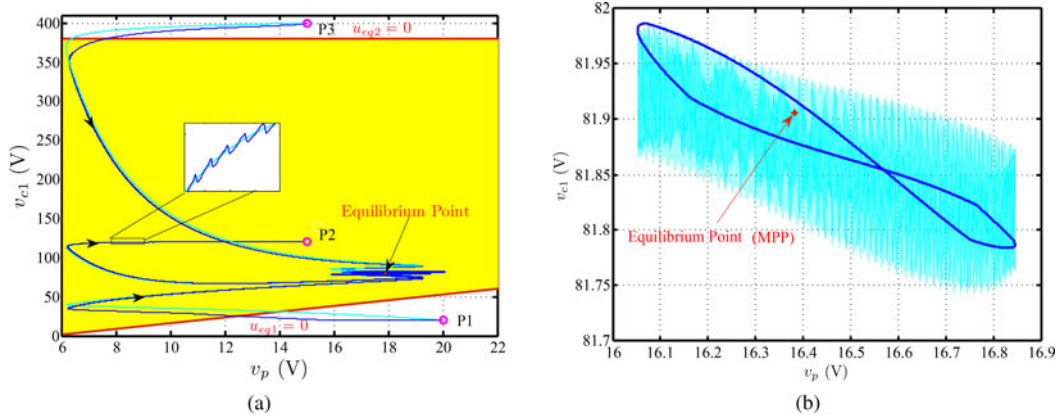


Fig. 11. Transient response of the system. (a) Trajectories from different initial conditions in the plane (v_p, v_{c1}) obtained from the full-order switched model and the ideal sliding-mode dynamics model. (b) Steady-state response in the plane (v_p, v_{c1}) from the full-order switched model and the reduced-order ideal sliding-mode dynamics model.

$r_{on2} = 165 \text{ m}\Omega$), and the internal resistances of the capacitors $r_{cp} = r_{c1} = 0.1\Omega$.

A. Numerical Simulation of the Proposed System

The validity of the ideal sliding-mode dynamics model has been checked in Fig. 11(a), where the trajectories of both the ideal sliding-mode and switched-mode model are shown. Three different initial condition points P1–P3 are considered, where the sliding-mode boundaries defined by $v_{c1} = v_{c1L}$ and $v_{c1} = v_{c1H}$, as defined in (24) and (25), are also plotted. It can be observed that the system trajectories converge to the limit cycle in the vicinity of the MPP in all the cases. For point P2, the ideal and switched-mode trajectories are in perfect agreement. For points P1 and P3, the mismatch between the ideal and switched trajectories is due to the fact that these points are outside the sliding-mode domain described previously. Fig. 11(b) shows the steady-state behavior of the system in the state plane (v_p, v_{c1}) using the full-order switched model and the reduced-order ideal sliding-mode dynamics model. The concordance between the results obtained from the different models is remarkable. Moreover, it can be noticed that the system converges to a limit cycle in the vicinity of the MPP in all the cases.

The steady-state time domain waveforms of the two cascaded boost-based LFRs using the ideal sliding-mode dynamics are depicted in Fig. 12. It can be noticed that the output voltage and the output current for the PV module have triangular waveforms and they are 180° out of phase. The frequency of the instantaneous power p is twice the frequency of the current or voltage. Therefore, each half period of the current or voltage, the maximum value of the power p is reached.

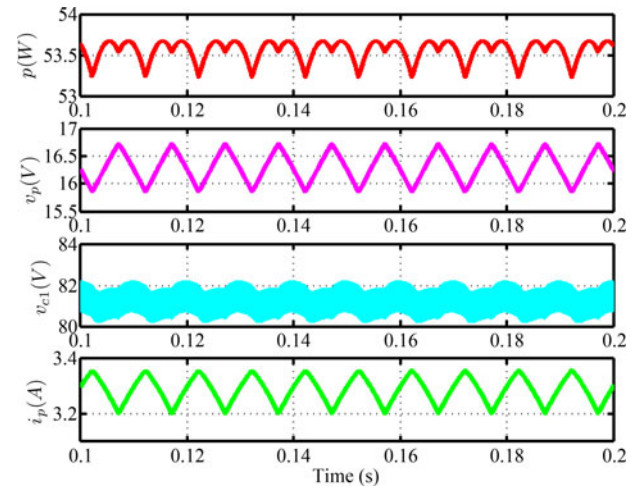


Fig. 12. Steady-state waveforms for the two cascaded converters behaving as LFRs supplied from a PV module operating with an MPPT controller.

The response of the two cascaded boost-based LFRs connected to the PV module with an MPPT have been checked also under the change of temperature T and irradiance S in Fig. 13. Fig. 13(a) depicts the response under step change of temperature with the same irradiance $S = 700 \text{ W/m}^2$. When the temperature increases from 25°C to 45°C , the power decreases but the system still works at the MPP for this temperature. Similarly, Fig. 13(b) illustrates the response of the system under a step irradiance change from $S = 700 \text{ W/m}^2$ to $S = 500 \text{ W/m}^2$ at constant temperature $T = 25^\circ\text{C}$. It can be noticed that the system is able to maintain the power in the vicinity of the MPP

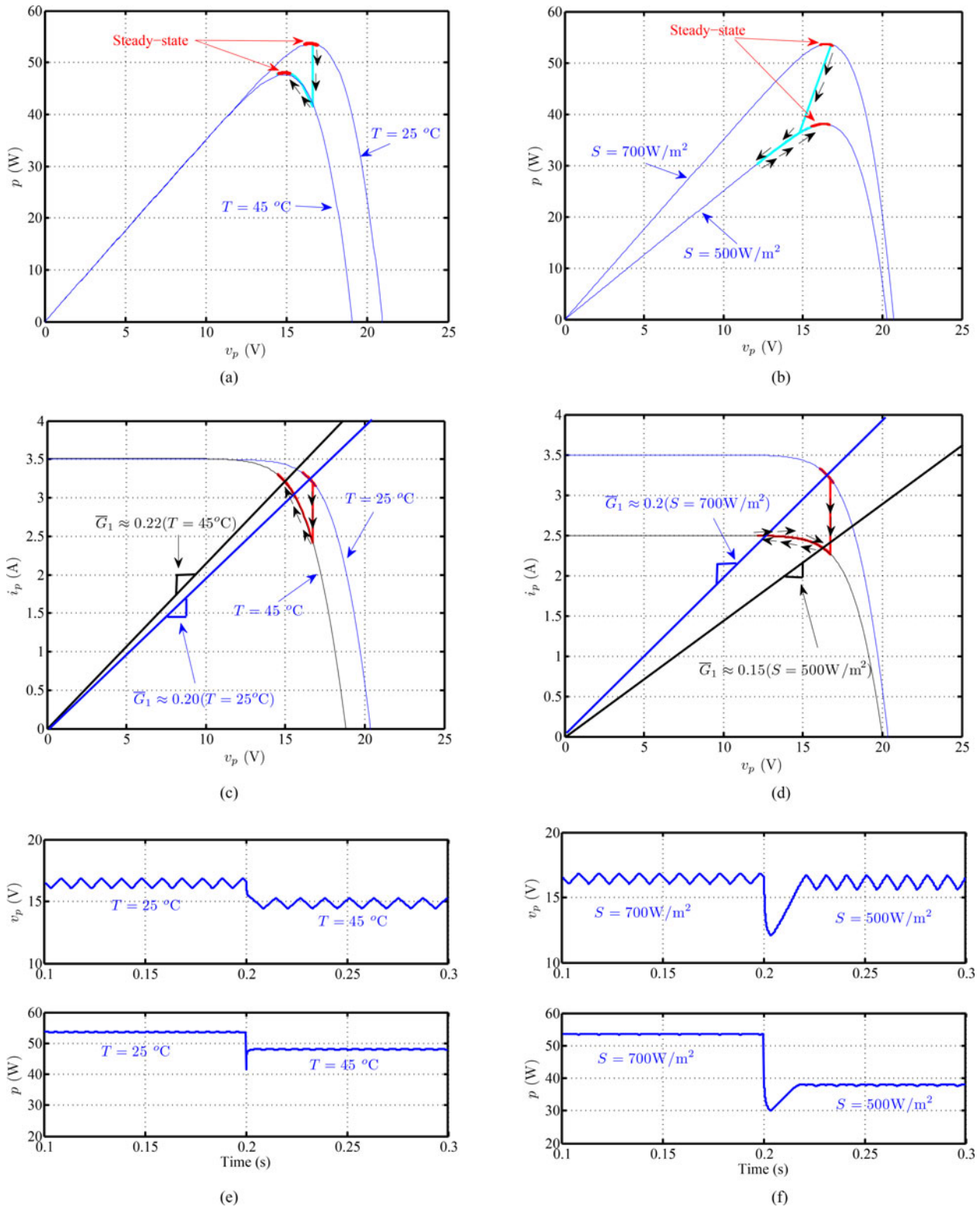


Fig. 13. Response of the cascaded LFR system supplied by the PV module with the MPPT controller under temperature and irradiance changes. (a) Temperature effect at $S = 700 \text{ W/m}^2$. (b) Irradiance effect at $T = 25^\circ\text{C}$. (c) Temperature effect at $S = 700 \text{ W/m}^2$. (d) Irradiance effect at $T = 25^\circ\text{C}$ (e) Temperature effect at $S = 700 \text{ W/m}^2$. (f) Irradiance effect at $T = 25^\circ\text{C}$.

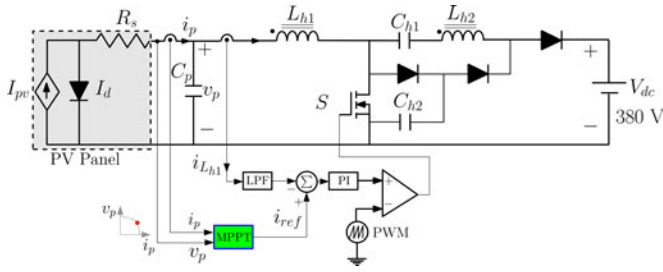


Fig. 14. Circuit diagram of the coupled-inductor high step-up converter of [20] with PI controller.

TABLE III
COUPLED-INDUCTOR CONVERTER [20] PARAMETERS

V_{dc}	L_{h1}	L_{h2}	C_p	C_{h1}	C_{h2}	G	τ_c	f_s
380 V	16 μ H	470 μ H	100 μ F	14 μ F	20 μ F	0.5	0.1 ms	50 kHz

under the variation of the external conditions. The PV $i-v$ characteristic curve and the LFR load line are depicted in Fig. 13(c) and (d) for the same step change in the temperature and irradiance, respectively. It can be noticed that when the temperature increases from 25 °C to 45 °C, the average conductance \bar{G}_1 changes from 0.2 S to 0.22 S to extract the maximum power as shown in Fig. 13(c). However, when the irradiance changes from $S = 700 \text{ W/m}^2$ to $S = 500 \text{ W/m}^2$, the conductance \bar{G}_1 changes from 0.2 S to 0.15 S for achieving the MPP steady-state for the new conditions as shown in Fig. 13(d). Therefore, the steady-state of the system for both irradiance levels is at the MPP. This can also be observed in the corresponding waveforms of v_p and p which are depicted in Fig. 13(e) and (f), respectively. It can be noticed that when the irradiance decreases, the power decreases while maintaining the operating point at the MPP. The previous tests confirm that this system is robust regardless of the change in temperature or irradiance.

B. Comparison of the Proposed Approach With a Previously Reported Solution [20]

This section presents a comparison that illustrates the advantages and limitations of the proposed converter and control approach. As mentioned in Section I there exists extensive literature in high-gain conversion topologies. The coupled-inductor single-stage solution proposed in [20] and [21] has been chosen for the comparison. This coupled-inductor converter was shown to deal with the same problem of interfacing PV modules with a high dc voltage in [21], and has the benefits of high efficient power conversion with only one controllable switch.

The coupled-inductor converter, which is shown in Fig. 14, using a conventional proportional integral (PI) controller scheme has been simulated in the same conditions of the previous section. The gain G and the time constant τ_c of the PI controller are mentioned in Table III. Similarly, the same ESC MPPT algorithm has been used to generate the reference for the current

controller. Table III shows the set of parameter values of the converter, which are the same that were reported in [21] with the exception of the input capacitance C_p . This parameter, which was equal to 3.3 mF in [21], has been reduced to 100 μ F in order to match the input capacitance of the cascaded boost converters.

Fig. 15 shows the waveforms of a transient simulation of the coupled-inductor and cascaded boost converters during a step change in irradiance at $t = 200 \text{ ms}$. It can be observed in the figure that the settling time of the cascaded boost converter is more than twice faster than the coupled-inductor converter. At the same time, the much larger input voltage and input current ripples of the coupled-inductor converter do not allow us to increase the MPPT gain because a higher deviation from the MPP would be expected under those conditions. It is worth to remark that a very large and bulky coupled inductance would be required in order to have a switching ripple similar to the one achieved with the cascaded boost converters.

Fig. 16 shows the two compared systems' response under a step change of the output voltage from 380 to 440 V. It can be noticed that increasing the output voltage has no effect on the input variables v_p and i_p of the PV module in the proposed system. However, in case of the coupled inductor single-stage converter, the change on the output voltage yields the interruption in the input voltage, input current, and extracted input power.

In terms of cost and size, the coupled-inductor converter requires three diodes, three capacitors, a MOSFET, and a coupled-inductor (i.e., two inductors on the same core). The cascaded boost converter needs two diodes, two capacitances, two MOSFETs, and two inductors, which for the same input current ripple, they will have smaller volume with respect to the coupled inductor. The proposed system presents lower volume and smaller number of components when compared with the high step-up gain converter. In general, the proposed system is more simple than the coupled inductor converter as regards the implementation or the stability analysis. As disadvantages, the cascaded boost converter requires some additional external circuitry for the sliding-mode control and some driving for the two MOSFETs, which presents a lower conversion efficiency.

V. EXPERIMENTAL RESULTS

Two cascaded boost converter prototypes connected to a BP585 PV module have been implemented in the laboratory. This PV module has a nominal power of 85 W [44]. A picture of the system and the PV module is shown in Fig. 18. The nominal values of the circuit parameters are the same that were shown in Table I. Current sensing is realized by means of an LA25-NP current transducer in both stages of the cascaded boost converters. The implementation of the prototypes has been carried out using Orcad program and the schematic diagram is depicted in Fig. 17, which has the reference of the used components. Note that this figure shows the power stage of the two cascaded boost converters and only the control of the first stage because the control of the second stage is similar.

A schottky diode is used for the first stage and a SiC diode is used for the second stage. The MPPT algorithm has been

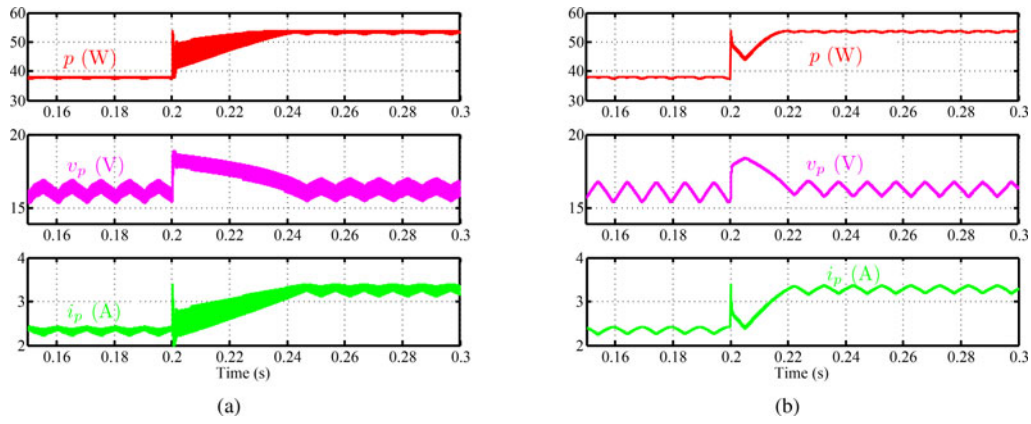


Fig. 15. Waveforms of the PV power, voltage, and current during an irradiance change from $S = 500 \text{ W/m}^2$ to $S = 700 \text{ W/m}^2$ at constant temperature 25°C . (a) Coupled-inductor converter. (b) Two cascaded boost converters.

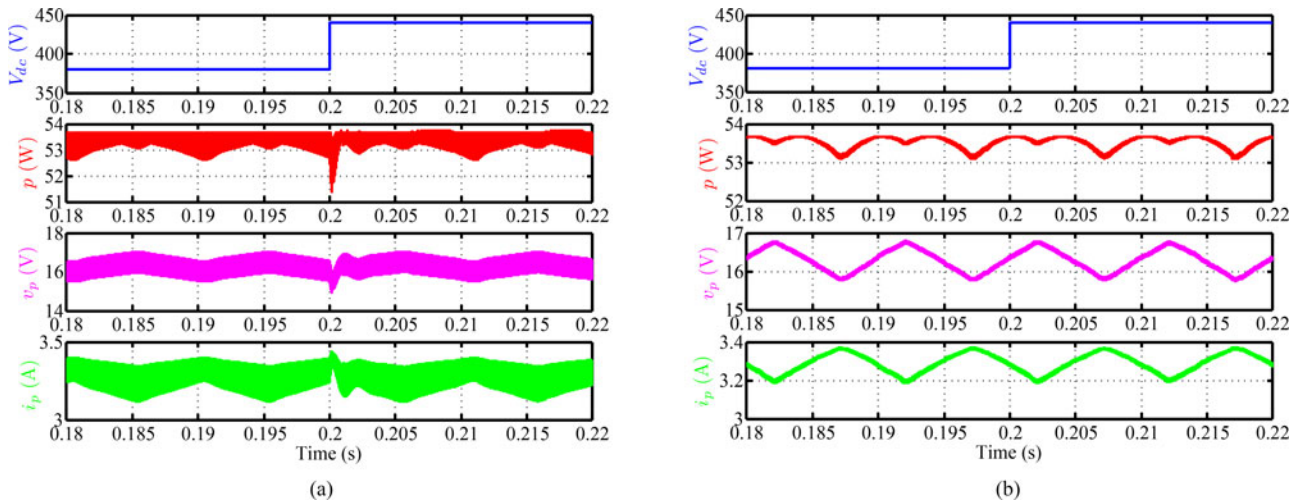


Fig. 16. Waveforms of the PV power, voltage, and current during an output voltage change from 380 to 440 V at constant temperature 25°C . (a) Coupled-inductor converter. (b) Two cascaded boost converters.

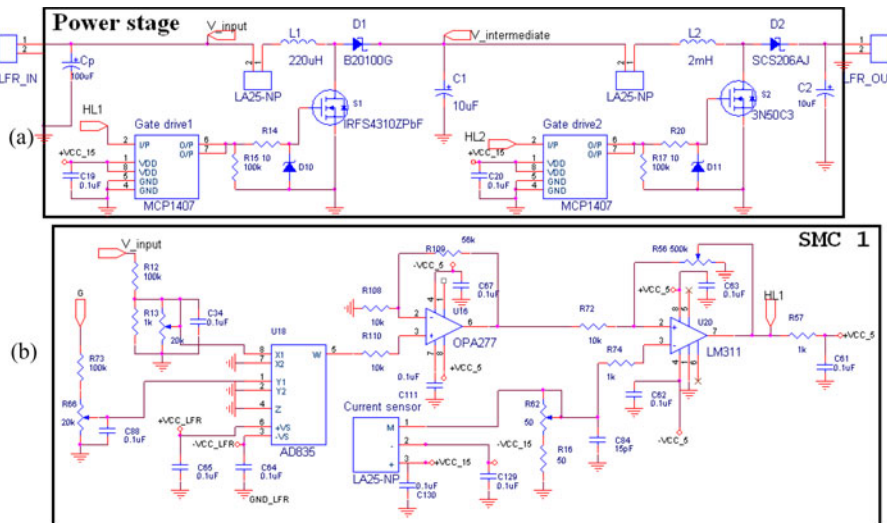


Fig. 17. Schematic diagram of the orcad program of the two cascaded boost-based LFRs using SMC. (a) Power stage of two cascaded boost converters. (b) Control of the first stage.

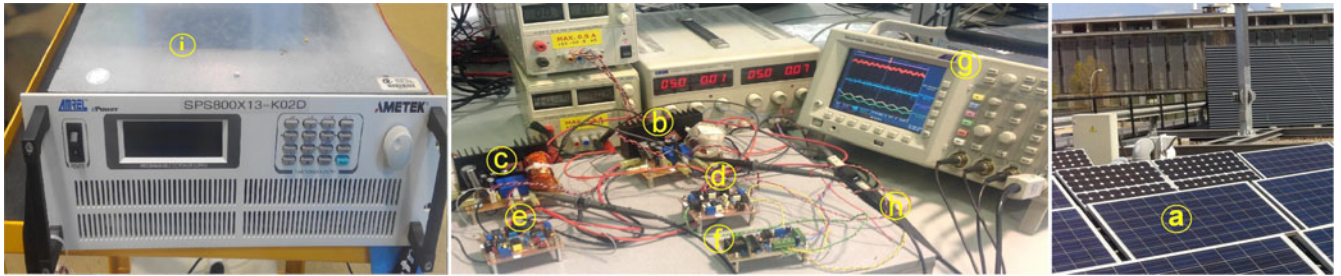


Fig. 18. Experimental prototypes for the two cascaded boost-based LFRs. (a) PV modules in the roof. (b) First stage LFR. (c) Second stage LFR. (d) SMC for the first stage. (e) SMC for the second stage. (f) MPPT controller. (g) Tektronix oscilloscope TDS3014C. (h) Tektronix probe (TCP202). (i) Load (380 V dc bus) SPS800X13.

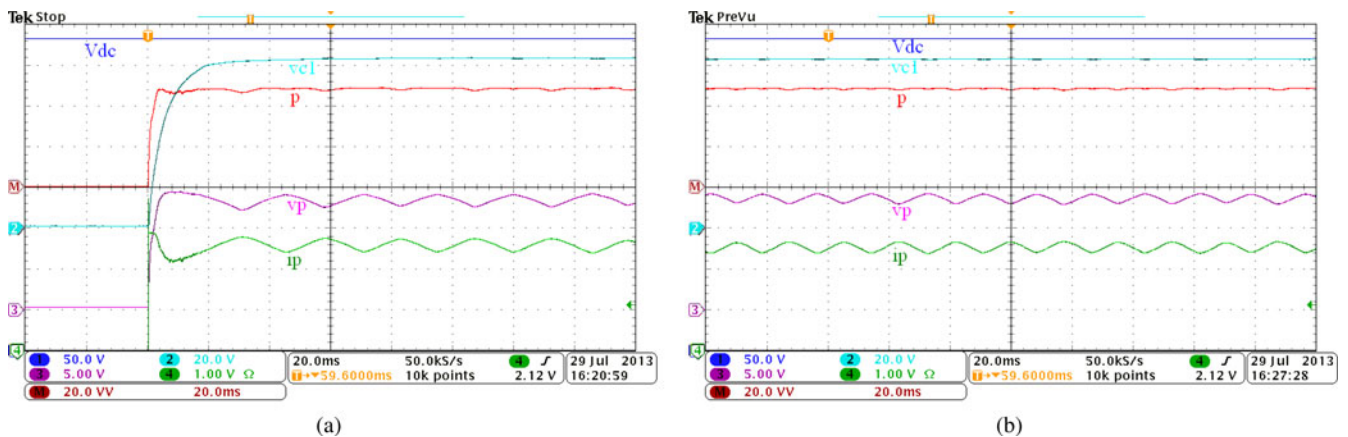


Fig. 19. Experimental waveforms of the two cascaded converters behaving as LFRs supplied from a PV module operating with an MPPT controller corresponding to (a) startup and (b) steady-state.

implemented using the microcontroller PIC18F1320 and an external integrator circuit. The period of oscillation of the MPP tracker has been fixed by means of the integrator gain and the time delay τ_d . This delay period has been fixed to 5 ms taking into account the aforementioned settling time of the system and the presence of noise in the prototype [14], [15]. In turn, the integrator gain has been tuned in order to obtain a good tradeoff between the static MPPT efficiency and the tracking speed at both low and rated power levels. The output of the two cascaded boost converters is connected to a constant dc voltage as a load (SPS800X13) of 380 V.

A. Steady-State Results

In order to evaluate the cascaded system, efficiency measurements for three different input voltage within a range of output power were taken. The prototypes present efficiencies above 90% for a wide range of output powers and input voltages, achieving a peak efficiency close to 95% for a conversion ratio between output and input voltages above 25. It is worth to point out that it can be expected that both efficiency and power density would increase with the use of GaN devices in a near future, given their improved ON resistance and output capacitance, which would also allow a significant increase of the switching frequency.

B. Transient Results

The transient behavior of the PV module during startup is depicted in Fig. 19(a). The starting point of the PV module is at zero current and open-circuit voltage 20 V. The voltage of the module decreases during the startup while the current and the power increase. It can be noticed that the settling time is small and that the system behaves as an LFR at steady-state. Fig. 19(b) shows the behavior of the different variables around the equilibrium. It can be observed that the slope change in both current and voltage takes place between the two maximum of power because the frequency of the power is twice the frequency of these variables.

The system has been tested under several disturbances. Fig. 20(a) shows the system response under a step change of the output voltage from 380 to 420 V. It can be noticed that increasing the output voltage has no effect on the input variables v_p and i_p of the PV module and consequently it does not alter the tracking of the input power, given the inherent power source characteristic of the LFRs that has been previously discussed in Section II-A. However, because of the losses, a small increase in the intermediate voltage v_{c1} can be noticed. Similarly, Fig. 20(b) shows the system response under a decrease of the output voltage. It can be noticed that, in this case, no effect on the PV power tracking can be observed.

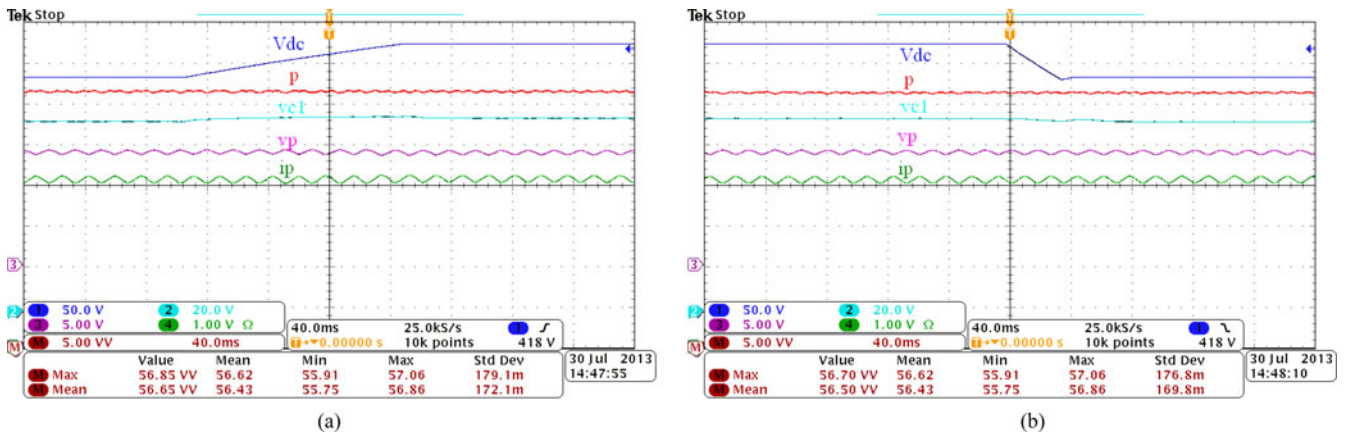


Fig. 20. Experimental waveforms of the system showing the effect of load changes. (a) Load increase from 380 V to 420 V. (b) Load decrease from 420 V to 380 V.

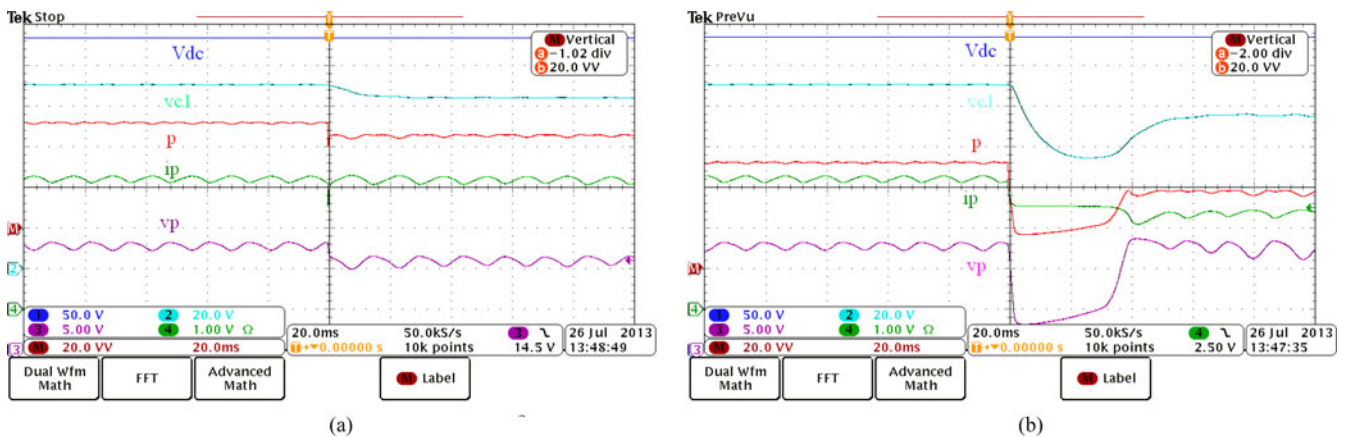


Fig. 21. Experimental waveforms of the system showing the effect of irradiance and temperature changes. (a) Temperature effect at $S = 700 \text{ W/m}^2$. (b) Irradiance effect at $T = 25^\circ\text{C}$.

The system has been also tested under temperature T and irradiance S changes. In order to control such changing conditions, a PV emulator E4360A has been used as a source for the following measurements. Fig. 21(a) shows the response of the system under a step change of temperature with the same irradiance level $S = 700 \text{ W/m}^2$. When the temperature increases from 25°C to 45°C , the power decreases but the system converges to the MPP for this temperature after a short transient period of about 20 ms. On the other hand, Fig. 21(b) shows the response under a step change of irradiance with the same temperature $T = 25^\circ\text{C}$. When the irradiance decreases from 700 to 500 W/m^2 , the power decreases but the system steady state is at the MPP for this temperature after a small transient time of about 30 ms.

VI. CONCLUSION

High-voltage conversion ratios can be achieved by using a cascade connection of dc–dc boost converters, in order to step up the low voltage of a PV module to the dc voltage of the grid (380 V). This cascade connection can be robustly controlled with a sliding-mode scheme imposing an LFR, such that the in-

put current is proportional to the input voltage. The operation of the circuit has been analyzed theoretically and with numerical simulations using the PV and MPPT models which are plugged in the ideal sliding-mode dynamic model. This model, which has been validated by using the full-order switched model, has the advantage of faster simulation time. Moreover, the ideal sliding-mode dynamic model allows us to develop a design-oriented description which facilitates the stability analysis of the system. This stability analysis shows that the system exhibits stable LFR characteristics without any conditions. Using the LFR canonical element with SMC in the cascade connection adds simplicity for the stability analysis and the implementation. The proposed system has been compared with a coupled-inductor converter reported in [20] in terms of dynamic performance, number of components, volume, and simplicity. While the coupled-inductor converter achieves slightly larger conversion efficiencies, the proposed system provides improved dynamic properties and higher reliability. The experimental tests carried out in the laboratory for the proposed system are in good agreement with the theoretical predictions and show that the extraction of the maximum power can be achieved robustly even

in the presence of climate (temperature or irradiance) or load changes. Finally, with the proposed system, a high conversion ratio can be achieved together with very fast tracking speed, high efficiency for the converters, and high static MPPT efficiency, which allows us to obtain the maximum available energy from the PV module.

REFERENCES

- [1] A. Cellatoglu and K. Balasubramanian, "Renewable energy resources for residential applications in coastal areas: A modular approach," in *Proc. 42nd Southeastern Symp. Syst. Theory*, Mar. 2010, pp. 340–345.
- [2] S. Luo and I. Batarseh, "A Review of distributed power systems part I: DC distributed power system," *IEEE Aerosp. Electron. Syst. Mag.*, vol. 20, no. 8, pp. 5–16, Aug. 2005.
- [3] B. Fahimi, A. Kwasinski, A. Davoudi, R. S. Balog, and M. Kiani, "Powering a more electrified planet," *IEEE Power Energy Mag.*, vol. 11, no. 2, pp. 54–64, Aug. 2011.
- [4] A. Sannino, G. Postiglione, and M. H. J. Bollen, "Feasibility of a DC network for commercial facilities," *IEEE Trans. Ind. Appl.*, vol. 39, no. 5, pp. 1499–1507, Sep. 2003.
- [5] D. Nilsson, "DC distribution systems," Ph.D. dissertation, Department of Energy and Environment, Chalmers Univ. Technol., Gothenburg, Sweden, 2005.
- [6] C. Xu and K. Cheng, "A survey of distributed power system—AC versus DC distributed power system," in *Proc. 4th Int. Conf. Power Electron. Syst. Appl.*, Jun. 2011, pp. 1–12.
- [7] Y.-C. Chang, C.-L. Kuo, K.-H. Sun, and T.-C. Li, "Development and operational control of two-string maximum power point trackers in DC distribution systems," *IEEE Trans. Power Electron.*, vol. 28, no. 4, pp. 1852–1861, Apr. 2013.
- [8] D. Boroyevich, I. Cvetkovic, D. Dong, R. Burgos, F. Wang, and F. Lee, "Future electronic power distribution systems a contemplative view," in *Proc. IEEE 12th Int. Conf. Optimization Elect. Electron. Equipment*, May 2010, pp. 1369–1380.
- [9] D. Salomonsson and A. Sannino, "Low-voltage DC distribution system for commercial power systems with sensitive electronic loads," *IEEE Trans. Power Del.*, vol. 22, no. 3, pp. 1620–1627, Jul. 2007.
- [10] P. Karlsson and J. Svensson, "DC bus voltage control for a distributed power system," *IEEE Trans. Power Electron.*, vol. 18, no. 6, pp. 1405–1412, Nov. 2003.
- [11] M. Brenna, G. Lazarou, and E. Tironi, "High power quality and DG integrated low voltage dc distribution system," in *Proc. IEEE Power Eng. Soc. General Meet.*, 2006.
- [12] G. R. Walker and P. C. Sernia, "Cascaded DC-DC converter connection of photovoltaic modules," *IEEE Trans. Power Electron.*, vol. 19, no. 7, pp. 1130–1139, Jul. 2004.
- [13] A. I. Bratcu, I. Munteanu, S. Bacha, D. Picault, and B. Raison, "Cascaded DC-DC converter photovoltaic systems: power optimization issues," *IEEE Trans. Ind. Electron.*, vol. 58, no. 2, pp. 403–411, Feb. 2011.
- [14] C. Sullivan, J. Awerbuch, and A. Latham, "Decrease in photovoltaic power output from ripple: Simple general calculation and the effect of partial shading," *IEEE Trans. Power Electron.*, vol. 28, no. 2, pp. 740–747, Feb. 2013.
- [15] A. Latham, R. Pilawa-Podgurski, K. Odame, and C. Sullivan, "Analysis and optimization of maximum power point tracking algorithms in the presence of noise," *IEEE Trans. Power Electron.*, vol. 28, no. 7, pp. 3479–3494, Jul. 2013.
- [16] G. Petrone, G. Spagnuolo, R. Teodorescu, M. Veerachary, and M. Vitelli, "Reliability issues in photovoltaic power processing systems," *IEEE Trans. Ind. Electron.*, vol. 55, no. 7, pp. 2569–2580, Jul. 2008.
- [17] R. J. Serna, B. J. Pierquet, J. Santiago, and R. C. Pilawa-Podgurski, "Field measurements of transient effects in photovoltaic panels and its importance in the design of maximum power point trackers," in *Proc. 28th Annu. IEEE Appl. Power Electron. Conf. Expo.*, Mar. 2013, pp. 3005–3010.
- [18] S. Kjaer, J. Pedersen, and F. Blaabjerg, "A review of single-phase grid-connected inverters for photovoltaic modules," *IEEE Trans. Ind. Appl.*, vol. 41, no. 5, pp. 1292–1306, Sep./Oct. 2005.
- [19] Q. Zhao and F. Lee, "High-efficiency, high step-up DC-DC converters," *IEEE Trans. Power Electron.*, vol. 18, no. 1, pp. 65–73, Jan. 2003.
- [20] R.-J. Wai and R.-Y. Duan, "High step-up converter with coupled-inductor," *IEEE Trans. Power Electron.*, vol. 20, no. 5, pp. 1025–1035, Sep. 2005.
- [21] R.-J. Wai, W.-H. Wang, and C.-Y. Lin, "High-performance stand-alone photovoltaic generation system," *IEEE Trans. Ind. Electron.*, vol. 55, no. 1, pp. 240–250, Jan. 2008.
- [22] B. Gu, J. Dominic, J.-S. Lai, Z. Zhao, and C. Liu, "High boost ratio hybrid transformer DC-DC converter for photovoltaic module applications," *IEEE Trans. Power Electron.*, vol. 28, no. 4, pp. 2048–2058, Apr. 2013.
- [23] M. A. Ismeil, A. Franceses, and R. Kennel, "Controller design for improved switched inductor (SL) Z-source inverter for photovoltaic applications," *Int. J. Adv. Renewable Energy Res.*, vol. 1, no. 6, pp. 345–353, 2012.
- [24] A. El Aroudi, R. Haroun, A. Kouzou, A. Cid-Pastor, and L. Martinez-Salamero, "A comparison between static and dynamic Performances of a Z-source and a dual-stage boost converter under SMC for PV energy applications," *Energy Procedia*, vol. 42, pp. 587–596, Nov. 2013.
- [25] R. D. Middlebrook, "Input filter consideration in design and application of switching regulators," in *Proc. IEEE Ind. Appl. Soc. Annu. Meet.*, 1976, pp. 366–382.
- [26] V. I. Utkin, *Sliding Modes and Their Application in Variable Structure Systems*. Moscow, Russia: MIR Publishers, 1978.
- [27] P. Mattavelli, L. Rossetto, G. Spiazzi, and P. Tenti, "General-purpose sliding-mode controller for DC/DC converter applications," in *Proc. 24th Annu. IEEE Power Electron. Spec. Conf.*, Jun. 1993, pp. 609–615.
- [28] R. Erickson and D. Maksimovic, *Fundamentals of Power Electronics*. New York, NY, USA: Springer, 2001.
- [29] R. Haroun, A. Cid-Pastor, A. El Aroudi, and L. Martinez-Salamero, "Synthesis of canonical elements for power processing in DC distribution systems using cascaded converters and sliding-mode control," *IEEE Trans. Power Electron.*, vol. 29, no. 3, pp. 1366–1381, Mar. 2014.
- [30] S. Vighetti, J. P. Ferrieux, and Y. Lembeye, "Optimization and design of a cascaded DC-DC converter devoted to grid-connected photovoltaic systems," *IEEE Trans. Power Electron.*, vol. 27, no. 4, pp. 2018–2027, Apr. 2012.
- [31] R. Haroun, A. El Aroudi, A. Cid-Pastor, G. Garcia, and L. Martinez-Salamero, "Large-signal modeling and stability analysis of two-cascaded boost converters connected to a PV Panel under SMC with MPPT," in *Proc. 39th Annu. Conf. IEEE Ind. Electron. Soc.*, Nov. 2013, pp. 949–954.
- [32] S. Singer and R. Erickson, "Canonical modeling of power processing circuits based on the POPI concept," *IEEE Trans. Power Electron.*, vol. 7, no. 1, pp. 37–34, Jan. 1992.
- [33] S. Singer, "Realization of loss-free resistive elements," *IEEE Trans. Circuits Syst.*, vol. 37, no. 1, pp. 54–60, Jan. 1990.
- [34] S. Singer and R. Erickson, "Power-source element and its properties," *IEEE Proc. Circuits, Devices Syst.*, vol. 141, no. 3, pp. 220–226, Jun. 1994.
- [35] L. Martinez-Salamero, "Synthesis of canonical elements for power processing," in *Proc. 6th Int. Multi-Conf. Syst., Signals Devices*, Mar. 2009, pp. 1–6.
- [36] G. R. Walker, "Evaluating MPPT converter topologies using a MATLAB PV model," *J. Elect. Electron. Eng., Australia*, vol. 21, no. 1, pp. 49–56, Jul. 2001.
- [37] M. Villalva, J. Gazoli, and E. Filho, "Comprehensive approach to modeling and simulation of photovoltaic arrays," *IEEE Trans. Power Electron.*, vol. 24, no. 5, pp. 1198–1208, May 2009.
- [38] G. Petrone, G. Spagnuolo, and M. Vitelli, "Analytical model of mismatched photovoltaic fields by means of lambert W-function," *Solar Energy Mater. Solar Cells*, vol. 91, no. 18, pp. 1652–1657, Dec. 2007.
- [39] J. Barrado, A. El Aroudi, H. Valderrama-Blavi, J. Calvente, and L. Martinez-Salamero, "Analysis of a self-oscillating bidirectional DC-DC converter in battery energy storage applications," *IEEE Trans. Power Del.*, vol. 27, no. 3, pp. 1292–1300, Jul. 2012.
- [40] T. Noguchi, S. Togashi, and R. Nakamoto, "Short-current pulse-based maximum-power-point tracking method for multiple photovoltaic-and-converter module system," *IEEE Trans. Ind. Electron.*, vol. 49, no. 1, pp. 217–223, Feb. 2002.
- [41] N. Femia, G. Petrone, G. Spagnuolo, and M. Vitelli, "Optimization of perturb and observe maximum power point tracking method," *IEEE Trans. Power Electron.*, vol. 20, no. 4, pp. 963–973, Jul. 2005.
- [42] M. A. G. de Brito, L. Galotto, L. P. Sampaio, G. de Azevedo e Melo, and C. A. Canesin, "Evaluation of the main MPPT techniques for photovoltaic applications," *IEEE Trans. Ind. Electron.*, vol. 60, no. 3, pp. 1156–1167, Mar. 2013.
- [43] R. Leyva, C. Alonso, I. Queinnec, A. Cid-Pastor, D. Lagrange, and L. Martinez-Salamero, "MPPT of photovoltaic systems using extremum-seeking control," *IEEE Trans. Aerosp. Electron. Syst.*, vol. 42, no. 1, pp. 249–258, Jan. 2006.
- [44] BP Solar BP585 Datasheet. (2003). [Online]. Available: <http://www.altestore.com/store/Solar-Panels/51-to-99-Watt-Solar-Panels/BP-Set-Of-10-Bp-Solar-Bp585-Solar-Panels/p3234/>.



Reham Haroun (S'09) was born in Egypt, in 1982. She received the Graduate degree in power and electrical engineering from the Aswan Faculty of Engineering, South Valley University, Aswan, Egypt, in 2004, and the master's degree from the same University in 2009. She is currently working toward the Ph.D. degree at Universitat Rovira i Virgili, Tarragona, Spain.

She worked as a Lecture Assistant at the South Valley University during the period 2004–2009. During the same period, she was a Member of Aswan

Power Electronics Application Research Center group. Her research interests include power electronics applications including dc–dc switched power supply and ac–dc power factor correction converters.



Abdelali El Aroudi (M'00) was born in Tangier, Morocco, in 1973. He received the Graduate degree in physical science from Faculté des sciences, Université Abdelmalek Essaadi, Tetouan, Morocco, in 1995, and the Ph.D. degree (Hons.) from Universitat Politècnica de Catalunya, Barcelona, Spain, in 2000.

During the period 1999–2001, he was a Visiting Professor at the Department of Electronics, Electrical Engineering and Automatic Control, Technical School of Universitat Rovira i Virgili, Tarragona,

Spain, where he became an Associate Professor in 2001 and a fulltime tenure Associate Professor in 2005. From September 2007 to January 2008, he was holding a Visiting Scholarship at the Department of Mathematics and Statistics, Universidad Nacional de Colombia, Manizales, Colombia, conducting research on modeling of power electronics circuits for energy management. From February 2008 to July 2008, he was a Visiting Scholar at the Centre de Recherche en Sciences et Technologies de Communications et de l'Informations, Reims, France. He has participated in three Spanish national research projects and five cooperative international projects. His research interests include structure and control of power conditioning systems for autonomous systems, power factor correction, stability problems, nonlinear phenomena, chaotic dynamics, bifurcations and control. He serves as usual reviewer for many scientific journals. He has published more than 150 papers in scientific journals and conference proceedings. He is a Member of the GAEI research group (Universitat Rovira i Virgili) on Industrial Electronics and Automatic Control whose main research fields are power conditioning for vehicles, satellites and renewable energy. He has given invited talks in several universities in Europe, South America, and Africa.



Angel Cid-Pastor (M'07) graduated as Ingeniero en Electrónica Industrial, in 1999, and as Ingeniero en Automática y Electrónica Industrial, in 2002, from Universitat Rovira i Virgili, Tarragona, Spain. He received the M.S. degree in the design of microelectronics and microsystems circuits from Institut National des Sciences Appliquées, Toulouse, France, in 2003. He received the Ph.D. degrees from Universitat Politècnica de Catalunya, Barcelona, Spain, and from Institut National des Sciences Appliquées, LAAS-CNRS, Toulouse, in 2005 and 2006,

respectively.

He is currently an Associate Professor at the Departament d'Enginyeria Electrónica, Eléctrica i Automática, Escola Tècnica Superior d'Enginyeria, Universitat Rovira i Virgili. His research interests include power electronics and renewable energy systems.



Germain Garcia (M'94) received the Diploma degree in engineering from the Institut National des Sciences Appliquées (INSAT), Toulouse, France, in 1984. He also received the Ph.D. degree in automatic control from the Institut National des Sciences Appliquées, Toulouse, in 1988, and the Habilitation a Diriger des Recherches, in 1997, from the same university.

He is currently at the LAAS-CNRS as a Full Professor of INSAT. His research interests include robust control theory, linear matrix inequalities, constrained control, and singularly perturbed models.



Carlos Olalla (S'06–M'09) received the M.S. degree in electronic engineering from Universitat Rovira i Virgili, Tarragona, Spain, in 2004, and the Ph.D. degree in advanced automatic control from Universitat Politècnica de Catalunya, Barcelona, Spain, in 2009.

In 2007 and 2009, he was a Visiting Scholar at the Laboratoire d'Analyse et d'Architecture des Systèmes, Toulouse, France, where he also held a Postdoctoral position until March 2010. From 2010 to 2012, he was a Visiting Scholar and a Research Associate at the Colorado Power Electronics Center), University of Colorado, Boulder, CO, USA. Since 2013, he has been a Research Associate at the Department of Electrical, Electronics and Automatic Control Engineering, Universitat Rovira i Virgili, where he works on modeling, optimization, and robust control synthesis methods for power converters and renewable energy systems.



Luis Martinez-Salamero (SM'85) received the Ingeniero de Telecomunicación and Doctorate degrees from the Universidad Politècnica de Cataluña, Barcelona, Spain, in 1978 and 1984, respectively.

From 1978 to 1992, he taught circuit theory, analog electronics, and power processing at Escuela Técnica Superior de Ingenieros de Telecomunicación, Barcelona. During the academic year 1992–1993, he was a Visiting Professor at the Center for Solid State Power Conditioning and Control, Department of Electrical Engineering, Duke University,

Durham, NC, USA. He is currently a Full Professor at the Departamento de Ingeniería Electrónica, Eléctrica y Automática, Escuela Técnica Superior de Ingeniería, Universitat Rovira i Virgili, Tarragona, Spain. During the academic years 2003–2004 and 2010–2011, he was a Visiting Scholar at the Laboratoire d'Architecture et d'Analyse des Systèmes of the Research National Center, Toulouse, France. His research interests include structure and control of power conditioning systems for autonomous systems. He has published a great number of papers in scientific journals and conference proceedings and holds a U.S. patent on the electric energy distribution in vehicles by means of a bidirectional dc-to-dc switching converter. He is the Director of the GAEI research group on Industrial Electronics and Automatic Control whose main research fields are power conditioning for vehicles, satellites and renewable energy.

Dr. Martinez-Salamero was a Guest Editor of the IEEE TRANSACTIONS ON CIRCUITS AND SYSTEMS (1997) for the special issue on Simulation, Theory and Design of Switched-Analog Networks. He was a Distinguished Lecturer of the IEEE Circuits and Systems Society in the period 2001–2002.